Hydrodynamic modelling of large arrays of modularized floating structures with independent oscillations

Deqing Zhang[a,b], Zhi-Ming Yuan[b], Junfeng Du[a], Huajun Li[c, *]
[a] College of Engineering, Ocean University of China, Qingdao, 266100, PR China
[b] Department of Naval Architecture, Ocean & Marine Engineering, University of Strathclyde, Glasgow, G4 0LZ, UK
[c] Shandong Provincial Key Lab of Ocean Engineering, Ocean University of China, Qingdao, 266100, PR China

Abstract:

It is a challenging issue to fully consider the radiation interaction among floating bodies in a large array configuration. It requires large computational efforts to resolve the interaction matrix of floaters oscillating independently with 6 degrees of freedom (DoF). Obviously, when the distance between 2 floaters is large enough, their interaction will gradually vanish. It inspires the present study to investigate a cut-off radius, outside which the hydrodynamic interaction can be ignored. It should be noted that the computational efficiency and accuracy is a pair of contradictions: a large cut-off radius is always accompanied by a high accuracy, but requires more computational efforts, and vice versa. The objective of the present study is to quantify the interaction effect and to find an optimal cut-off radius which could reduce the computational time while ensuring a satisfactory accuracy in engineering practice. Based on the potential flow theory, we calculated the hydrodynamic interaction among multiple rectangular boxes and eventually quantified the interaction effects determined by the oscillating frequency and separating distance. Some critical curves of various truncation errors (*Et*) were obtained, showing whether the hydrodynamic interaction effects can be neglected, were depicted. The results from two case studies showed that the present cut-off scheme could provide a very reliable prediction of the hydrodynamic responses of multiple floating bodies in an array, while the computational time was significantly saved.

Keywords: modularized floating structures, radiation interaction, cut-off radius, truncation errors

1. Introduction

For offshore floating structures, arrays are usually composed of a few to hundreds of floaters deployed in the same geographic location and arranged systematically in ocean surface. The concept

This is a peer-reviewed, accepted author manuscript of the following article: Zhang, D., Yuan, Z-M., Li, H., & Du, J. (2022). Hydrodynamic modelling of large arrays of modularized floating structures with independent oscillations. Applied Ocean Research, 129, [103371]. https://doi.org/10.1016/j.apor.2022.103371

of arrays has been widely applied to many offshore engineering practice, e.g. very large floating structures (VLFS) and renewable energy farms including wave energy converters (WECs), floating photovoltaics (FPVs) and floating offshore wind turbine farms (FOWTs) (Rodrigues, 2021). The hydrodynamic behaviour could determine the optimum layout configurations for these arrays to ensure operational safety and maximize power extraction (Penalba et al., 2017). However, the total performance of these arrays is significantly affected by the hydrodynamic interactions between individual devices.

The hydrodynamic interaction problems have been studied since the 1970s, when Ohkusu (1976) used the 2-D strip theory to calculate the sway response of two parallel arranged structures. His analysis clearly showed the importance of the position: the weather and lee side. Kodan (1984) applied Ohuksu's method (1976) to analyze the hydrodynamic interaction between two parallel, slender, ship-shape structures in oblique waves. The good agreement between his results and the model tests illustrated that the 2-D strip theory was a simple and effective method for predicting the hydrodynamic interaction between two adjacent structures. However, due to the 2-D assumptions, some limitations, for instance, the overestimation of the interaction effect in some frequency ranges, still exist (Fang and Kim, 1986). With the development of computer technology and computational theory, the 3-D flow interaction methods began to play an important role. Hong et al. (2005) investigated the motion responses and drift forces of side-by-side moored multiple bodies using a higher-order boundary element method (HOBEM). They compared their numerical results with the model tests and got a good agreement. Zhu et al. (2008) used a 3-D time-domain Green function method to predict the gap influence on the wave forces of twin box-shaped floating bodies. By comparison with the results from the frequency domain technique, the results obtained from the time domain method was validated and revealed similar resonant phenomena and hydrodynamic interaction. Yuan et al. (2016) developed a frequency-domain code based on the 3-D Rankine source method to evaluate the hydrodynamic interaction between two ships advancing in waves. They validated their numerical predictions with the model test results carried out by Kashiwagi and Ohkusu (1991) and then depicted a diagram showing whether the ship-to-ship hydrodynamic interaction effects are expected.

Most of the published studies focused on the prediction of the hydrodynamic interactions between two or three bodies. The studies on large-size floaters are relatively rare due to the increasing complexity and computational cost of large number of interacting devices. Borgarino et al. (2012a) used a BEM tool to assess the influence of the separating distance between 9-25 heaving cylinders and surging barges. Their results clearly showed that the diffracted and radiated waves led to a sufficient increase in energy absorption. Engström et al. (2013) evaluated the power variation in an array of 32 point-absorbing WECs and summarized the smoothing effect due to the number of devices and their hydrodynamic interactions. It showed that the variance in power production depends crucially on the geometry of the array and the number of interacting devices. Yang et al. (2020) employed two 10-WEC models to investigate the hydrodynamic interactions on the fatigue damage of mooring lines. Their simulations showed that the predicted fatigue damage could be varied by more than tenfold.

The direct simulations with established techniques require large computational resources when the number of interacting bodies grows. Therefore, developing a fast approach to solve hydrodynamic interaction effects in large arrays is highly demanded. In some studies, the fast algorithms are designed to accelerate the hydrodynamic simulations, including the fast multipole method (FMM) (Utsunomiya and Watanabe, 2002; Teng and Gou, 2006; Borgarino et al., 2012b) and pre-corrected fast Fourier transforms (FFT) (Kring et al., 2000). However, there are many limitations of these approaches (Singh and Babarit, 2014). In FMM methods, the numerical convergence of the existing multipole series expansion of the free surface Green function is complex, while in FFT, the construction of a grid and projection operations over the whole domain of the sparse array will lead to a sub-optimal algorithm. Apart from the above-mentioned acceleration algorithms, some simplified techniques have also been developed. Budal (1977), Fizgerald and Thomas (2007) developed a point absorber method, in which the diffracted and radiated waves were ignored when calculating the optimal power absorption of an array regardless of individual WEC geometry. The plane wave approximation (Simon, 1982) combined with the BEM was developed by Singh and Babarit (2014) to investigate the wave interaction effects in sparse arrays. Göteman et al. (2015) used an approximate model, in which the scattered waves were neglected when optimizing the wave energy park geometries and configurations.

The present study develops a numerical method for fast hydrodynamic modelling of large arrays of modularized floating bodies by introducing an interaction cut-off scheme. The scheme makes it feasible to quickly determine the coupling range in which the hydrodynamic interaction effects should be modelled. The in-house developed numerical programme MHydro (Yuan et al., 2015), which is based on the 3-D Rankine source panel method, is used to estimate the critical lines showing whether the interaction should be considered in the computation. Then, two validations are carried out to investigate the effect of introducing an optimal cut-off radius in the calculations. The proposed cut-off scheme can also be implemented to other multi-body hydrodynamic interaction solvers.

2. Mathematical formulations of the potential theory

2.1 Coordinate systems

Considering *N* bodies oscillating independently in open sea, the right-handed coordinate systems defined in the present study are shown in Fig. 1. The global coordinate system *O-XYZ* is fixed on the undisturbed free surface, and *OZ* axis is positive upwards. o_m-$x_m y_m z_m$ (*m*=1, 2, …, *N*) are body coordinate systems with their origins locating on the mean free surface at midships and positive z_m axis pointing upwards. d_m and l_m represent the transverse and longitudinal distance between the *m*-th body coordinate system and the global coordinate system, respectively. The incident wave direction β is assumed as the angle between the wave propagation direction and *X*-axis, with $\beta = 180°$ defined as the head wave.

In the computation, the motions and forces are transferred to the local coordinate system in which the origin is placed at the centre of gravity of each body.

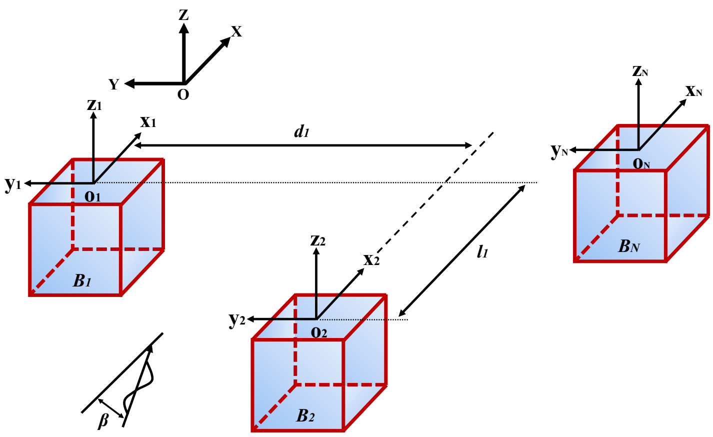

Fig. 1. Coordinate systems.

2.2 Boundary value problem

Assuming the incompressible and inviscid surrounding fluid with irrotational motion, the velocity potential which satisfies the Laplace equation in the whole fluid is introduced. The linearized velocity potential can be decomposed into

$$\Psi(\vec{X},t) = Re[\eta_0\varphi_0(\vec{X})e^{-i\omega_0 t}] + Re\sum_{j=1}^{6}\sum_{m=1}^{N}[\eta_j^m\varphi_j^m(\vec{X})e^{-i\omega_0 t}] + Re[\eta_7\varphi_7(\vec{X})e^{-i\omega_0 t}] \quad (1)$$

where *Re(*)* denotes the real part of the argument; *N* is the total number of modularized floating bodies; ω_0 is the incident wave frequency; φ_0 is the unit incident potential and $\eta_0 = \eta_7$ is the incident wave amplitude; φ_j^m (*j*=1, 2, …, 6, *m*=1, 2, …, *N*) is the unit radiated wave potential in 6 degrees of freedom (DoF) and η_j^m (*j*=1, 2, …, 6, *m*=1, 2 , …, *N*) is the corresponding oscillation amplitude (η_1: surge; η_2: sway; η_3: heave; η_4: roll; η_5: pitch; η_6: yaw); φ_7 is the unit diffracted wave potential.

The linearized incident wave velocity potential φ_0 is described as

$$\varphi_0 = -\frac{ig\eta_0}{\omega_0}\frac{\cosh k(z+d)}{\cosh kd}e^{i[k(x\cos\beta + y\sin\beta)]} \quad (2)$$

where β is the angle of wave heading; and *k* is the wave number that satisfies the dispersion relation

$$k \cdot \tanh kd = {\omega_0}^2/g \quad (3)$$

The governing equation and linearized boundary conditions used to solve the perturbation velocity potential φ_7 and φ_j^m (m=1, 2, …, N) are summarized as follows:

1) Diffraction wave potential

$$\nabla^2\varphi_7 = 0 \quad \text{in the fluid domain;} \tag{4}$$

$$g\frac{\partial\varphi_7}{\partial z} - {\omega_0}^2\varphi_7 = 0 \quad \text{on the undisturbed free surface } S_f; \tag{5}$$

$$\frac{\partial\varphi_7}{\partial n} = -\frac{\partial\varphi_0}{\partial n}|_{S_m} \quad \text{on the mean wetted body surface } S_m; \tag{6}$$

$$\frac{\partial\varphi_7}{\partial z} = 0 \quad \text{on the seabed.} \tag{7}$$

2) Radiation wave potential

$$\nabla^2\varphi_j^m = 0, \quad j = 1,2,\ldots,6 \quad \text{in the fluid domain;} \tag{8}$$

$$g\frac{\partial\varphi_j^m}{\partial z} - {\omega_0}^2\varphi_j^m = 0, \; j = 1,2,\ldots,6 \quad \text{on the undisturbed free surface } S_f; \tag{9}$$

$$\frac{\partial\varphi_j^m}{\partial n} = \begin{cases} -i\omega_0 n_j|_{S_m} \\ 0|_{S_{others}} \end{cases}, \quad j = 1,2,\ldots,6 \quad \text{on the mean wetted body surface } S_m \text{ (} B_m \text{ is oscillating while others are fixed);} \tag{10}$$

$$\frac{\partial\varphi_j^m}{\partial z} = 0 \quad \text{on the seabed.} \tag{11}$$

Moreover, a suitable Sommerfeld radiation condition must be imposed on the control surface to complete the above boundary value problem. The generalized normal vectors are expressed as

$$n_j = \begin{cases} \boldsymbol{n}, & j = 1,2,3 \\ \boldsymbol{x} \times \boldsymbol{n}, & j = 4,5,6 \end{cases} \tag{12}$$

where $\boldsymbol{n} = (n_1, n_2, n_3)$ is the unit normal vector directed inward on body surface S_m; $\boldsymbol{x} = (x, y, z)$ is the position vector on S_m.

2.3 Equations of motion

Once the velocity potentials φ_j^m are obtained, the pressure on each body surface can be computed directly from Bernoulli's equation:

$$p_j^m = -i\omega\rho\varphi_j^m, \quad j = 0,1,\ldots,6,7; \; m = 1,2,\ldots,N \tag{13}$$

where ρ is the fluid density.

The wave excitation force can then be obtained by integrating the incident and diffraction pressure on the wetted body surface as follows:

$$F_i^{W_m} = \iint_{S_m} (p_0 + p_7)\, n_i dS \tag{14}$$

Furthermore, the hydrodynamic forces produced by the oscillatory motion of B_m in the i_{th} direction can be expressed as

$$F_i^{R_m} = \sum_{j=1}^{6} \iint_{S_m} p_j^m\, n_i dS \cdot \left(\sum_{n=1}^{N} \eta_j^n \right) = \sum_{j=1}^{6} \sum_{n=1}^{N} (\omega_0^2 \mu_{ij}^{mn} + i\omega_0 \lambda_{ij}^{mn}) \eta_j^n \,, i = 1, 2, \dots, 6;\ m = 1, 2, \dots, N \tag{15}$$

where μ_{ij}^{mn} is the added mass coefficient of B_m in the i_{th} mode which is induced by the oscillation motion of B_n in the j_{th} mode; λ_{ij}^{mn} is the damping coefficient in which the definitions of subscript and superscript are the same as those of added mass. The added mass and damping coefficients can be written as

$$\mu_{ij}^{mn} = -\frac{\rho}{\omega_0} \iint_{S_m} \varphi_{Ij}^n\, n_i dS, \qquad i, j = 1, 2, \dots, 6;\ m, n = 1, 2, \dots, N \tag{16}$$

$$\lambda_{ij}^{mn} = -\rho \iint_{S_m} \varphi_{Rj}^n\, n_i dS, \qquad i, j = 1, 2, \dots, 6;\ m, n = 1, 2, \dots, N \tag{17}$$

where φ_{Ij} donates the imaginary part of j_{th} radiation potential, and φ_{Rj} is the real part.

Based on Newton's second law, the body motions in the frequency domain can be obtained by

$$\sum_{j=1}^{6} \left\{ [-\omega_0^2 (M_{ij}^m + \mu_{ij}^{mm}) + i\omega_0 \lambda_{ij}^{mm} + K_{ij}^m] \eta_j^m + \sum_{\substack{n=1 \\ n \neq m}}^{N} (-\omega_0^2 \mu_{ij}^{mn} + i\omega_0 \lambda_{ij}^{mn}) \eta_j^n \right\} = F_i^{W_m}, \qquad i, j = 1, 2, \dots, 6;\ m, n = 1, 2, \dots, N \tag{18}$$

where M_{ij}^m is the generalized mass matrix for B_m; and K_{ij}^m is the restoring matrix.

The wave elevation of the free surface then can be obtained from the dynamic free surface boundary condition in the form

$$\zeta_j = \frac{i\omega_0}{g} \sum_{m=1}^{N} \eta_j^m \varphi_j^m = \zeta_{Rj} + i\zeta_{Ij}, \qquad j = 0, 1, \dots, 7; m = 1, 2, \dots, N \tag{19}$$

where ζ_{Rj} donates the real part of *j*-th mode, and ζ_{Ij} is the imaginary part.

2.4 Numerical implementation

The whole computational domain is composed of the body-, free-, control- surface and seabed. In the numerical study, the boundary of the computational domain is discretized into a number of quadrilateral panels with different source density $\sigma(\xi)_j$, where $\xi = (\xi, \eta, \varsigma)$ is the position vector on the boundary. If $\boldsymbol{x} = (x, y, z)$ is the filed point, the velocity potential can be written as

$$\varphi(\boldsymbol{x})_j = \iint_{S_b+S_f+S_c} G(\boldsymbol{x}, \boldsymbol{\xi})\, \sigma(\boldsymbol{\xi})_j\, dS_\xi, \qquad j = 1, 2, \ldots, 7 \tag{20}$$

where $G(\boldsymbol{x}, \boldsymbol{\xi})$ is the Rankine-type Green function that satisfies the impenetrable seabed boundary condition through the method of mirror image

$$G(\boldsymbol{x}, \boldsymbol{\xi}) = \frac{1}{\sqrt{(x-\xi)^2 + (y-\eta)^2 + (z-\varsigma)^2}} + \frac{1}{\sqrt{(x-\xi)^2 + (y-\eta)^2 + (z+2d+\varsigma)^2}} \tag{21}$$

Particular attention should be paid to the influence coefficients $G(\boldsymbol{x}, \boldsymbol{\xi})$. Generally, Eq. (21) is valid when the distance between two panels is large. However, when two panels are too close to each other, the value of influence coefficients $G(\boldsymbol{x}, \boldsymbol{\xi})$ should be evaluated by computing the analytical formulas summarized by Prins (1995). Moreover, the first derivatives of the velocity potential can be obtained from the analytical formulas listed by Hess and Smith (1964).

The singularity is required to be distributed precisely on the boundary of the computational domain in the classical Rankine source method. In practice, the singularity distribution can be located at a short distance above the free surface, as shown in Fig. 2, as long as the collocation points remain on the free surface and the boundary condition is still satisfied at these points (Cao et al., 1987). It can lead to the ill-conditioning of the algebraic system if the raised distance is not correctly chosen. In the present study, the raised distance $\Delta z_i = \sqrt{S_i}$ suggested by Yuan et al. (2014) is selected, where S_i is the area of the *i*-th panel.

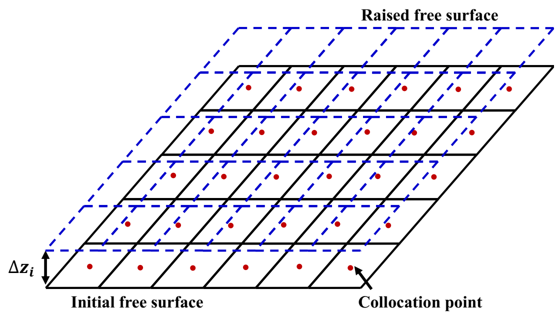

Fig. 2. Sketch of the raised mesh on the free surface.

3. Interaction cut-off scheme

Large arrays usually consist of hundreds of individual modularized bodies, which requires significant computational resources to resolve the radiation interactions among them. In the present numerical model, the most computationally intensive part is to obtain the radiation velocity potential components $\varphi(\mathbf{x})_j$ (j=1, 2, …, 6) by calculating the source density $\sigma(\boldsymbol{\xi})_j$, where j represents 6 DoF. As shown in Eq. (20), the size of the source density matrix needs to be computed is $6 \times Q$ when one floater is oscillating independently in 6 DoF while others are fixed, where Q is the number of panels on the boundary. Each source density parameter $\sigma(\boldsymbol{\xi})_j$ in these matrices is non-zero. For an array of N bodies, a total number of $6 \times Q^2 \times N$ velocity potentials must be obtained to solve the boundary value problem, which poses a challenging computational task as the array size increases.

In this paper, a numerical scheme is proposed to reduce the computational cost by neglecting the coupling terms of the radiation velocity potential when the distance between m- and n-th body is sufficiently large. The distance between two floating structures refers to the distance between the centroids of the two bodies. In a 2-bodies array, it is obvious that when the position of the first body B_1 is fixed and the distance between the two bodies B_1 and B_2 is a constant value d, the position of the second body B_2 is various. However, the second body B_2 can only be arranged on the boundary of a circle with the first body B_1 as the center and with the determined distance d as the radius. Similarly, when the local coordinate system is fixed on one body and the truncation distance is determined to be a certain value, it is reasonable that the truncation scope is specified as a circle. Fig. 3 shows how to determine whether the coupled radiation hydrodynamic coefficients φ^{mn} should be calculated. The different solid points represent the positions of the different floating bodies. Under the m-th local coordinate system fixed on the ~~m-th~~ body located at the red point, we define a truncation range with the red point as the center of the circle and the truncation distance as the radius.~~we define a cut-off radius R, as shown in the sketch in Fig. 3, within which the radiation interaction needs to be considered.~~ If the n-th body is located outside ~~this radius~~the cut-off circle, the coupling terms φ_j^{mn} are neglected. Also, the body located at the green point or at the yellow point will only be calculated for the interaction with other floaters located inside its cut-off circle. It is worth noting that in a N-

Formatted: Font: (Asian) +Body Asian (DengXian), English (UK), Pattern: Clear
Formatted: Font: (Asian) +Body Asian (DengXian), English (UK), Pattern: Clear
Formatted: Font: (Asian) +Body Asian (DengXian), English (UK), Pattern: Clear
Formatted: Font: (Asian) +Body Asian (DengXian), English (UK), Pattern: Clear
Formatted: Font: (Asian) +Body Asian (DengXian), English (UK), Pattern: Clear
Formatted: Font: (Asian) +Body Asian (DengXian), English (UK), Pattern: Clear
Formatted: Font: (Asian) +Body Asian (DengXian), English (UK), Pattern: Clear
Formatted: Font: (Asian) +Body Asian (DengXian), English (UK), Pattern: Clear
Formatted: Font: (Asian) +Body Asian (DengXian), English (UK), Pattern: Clear
Formatted: Font: (Asian) +Body Asian (DengXian), English (UK), Pattern: Clear
Formatted: Font: (Asian) +Body Asian (DengXian), English (UK), Pattern: Clear
Formatted: Font: (Asian) +Body Asian (DengXian), English (UK), Pattern: Clear
Formatted: Font: (Asian) +Body Asian (DengXian), English (UK), Pattern: Clear
Formatted: Font: (Asian) +Body Asian (DengXian), English (UK), Pattern: Clear
Formatted: Font: (Asian) +Body Asian (DengXian), English (UK), Pattern: Clear
Formatted: Font: (Asian) +Body Asian (DengXian), English (UK), Pattern: Clear
Formatted: Font: (Asian) +Body Asian (DengXian), English (UK), Pattern: Clear
Formatted: Font: (Asian) +Body Asian (DengXian), English (UK), Pattern: Clear
Formatted: Font: (Asian) +Body Asian (DengXian), English (UK), Pattern: Clear
Formatted: Font: (Asian) +Body Asian (DengXian), English (UK), Pattern: Clear
Formatted: Font: (Asian) +Body Asian (DengXian), English (UK), Pattern: Clear
Formatted: Font: (Asian) +Body Asian (DengXian), English (UK), Pattern: Clear
Formatted: Font: (Asian) +Body Asian (DengXian), English (UK), Pattern: Clear
Formatted: Font: (Asian) +Body Asian (DengXian), English (UK), Pattern: Clear
Formatted ... [1]
Formatted: Font: (Default) Times New Roman
Formatted: Font: (Default) Times New Roman
Formatted: Font: (Default) Times New Roman
Formatted: Font: (Default) Times New Roman, Italic
Formatted: Font: (Default) Times New Roman

bodies array, *N* truncation scopes will be defined with each floater as the center and the same truncation distance as the radius. Obviously, a smaller radius is desired for a fast computation. However, it may be accompanied by a larger truncation error (*Et*). The cut-off radius associated with the *Et* is determined by a few parameters, including the wave frequency, the modular shape and configuration, and the accuracy requirement. Generally, the floating structures which could compose a large array have the same shape and size to facilitate construction, installation and arrangement. To find the optimal cut-off radius, it requires extensive simulations of an array of two bodies with the same modular shape in advance. Once the optimal cut-off radius is selected, it can be applied repeatedly to optimize the array layout with minimum computational efforts.

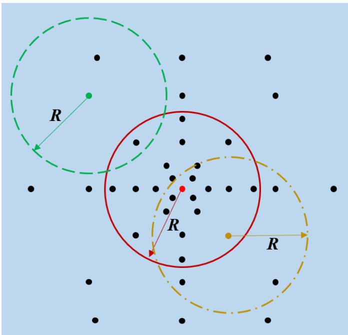

Fig.3. Sketch of the truncation scope of the radiation interaction, taking the three bodies at the red, green and yellow points as examples, respectively. The different solid points represent the positions of the different floating bodies. The truncation distance is determined as *R*.

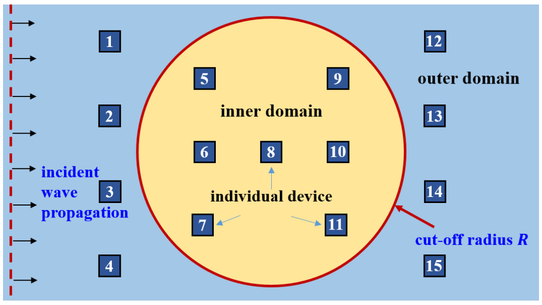

Fig. ~~3~~4. An example of the cut-off scheme for arrays of modularized floating structures. The radiation interaction in the inner domain is considered in the calculation, while in the outer domain it is ignored.

Formatted: Font: (Default) Times New Roman, Italic
Formatted: Font: (Default) Times New Roman
Formatted: Font colour: Text 1, English (UK), Pattern: Clear
Formatted: Font colour: Text 1, English (UK), Pattern: Clear
Formatted: Indent: First line: 0 ch, Line spacing: single
Formatted: Font colour: Text 1, English (UK), Pattern: Clear
Formatted: Font: 10.5 pt, Font colour: Text 1

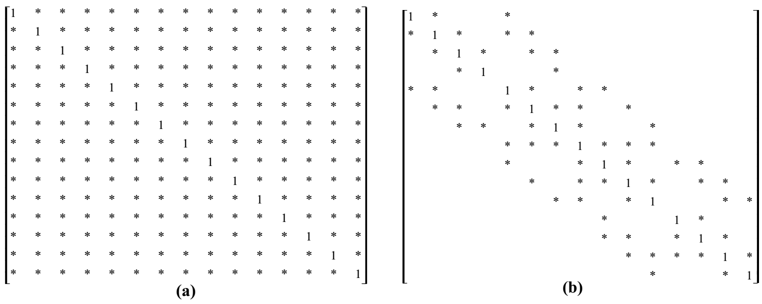

Fig. 45. Radiation interaction matrix of a 15-bodies array. (a) Full rank matrix considering hydrodynamic interactions between all devices; (b) Sparse matrix introducing interaction coupling radius cut-off.

Fig. 4 5 shows the radiation interaction matrix of an array consisting of 15 modularized bodies that shown in Fig. 34. Theoretically, each body is oscillating independently in 6 DoF. The total unknow element number of the full radiation interaction matrix is 6×15^2, indicating we have to solve the coupling terms φ_j^{mn} 1,350 times independently to obtain the radiation hydrodynamic properties of the array. However, as shown in Fig. 3 4 and Fig. 45(b), if the distance between *m*- and *n*-th floater is greater than the defined cut-off radius *R*, the coefficient located in the *m*-th row, *n*-th column of the radiation interaction matrix will be ignored. Therefore, the radiation interaction matrix will be sparse if a cut-off scheme is applied, and the unknown element number is reduced to 6×78. It explains how the computational cost is reduced. It can be imagined that when the size of the array increases, more computational time can be saved, which enables a feasible modelling of the hydrodynamic properties of large array of floaters.

Fig.5 6 is the flow chart of the hydrodynamic modelling for arrays with implementation of a radius cut-off scheme. The diffraction problem is solved with a standard procedure. The cut-off scheme is mainly introduced to save the time for the radiation problem. We will quantify the *Et*, as well as the improvement in computational efficiency in the next sections.

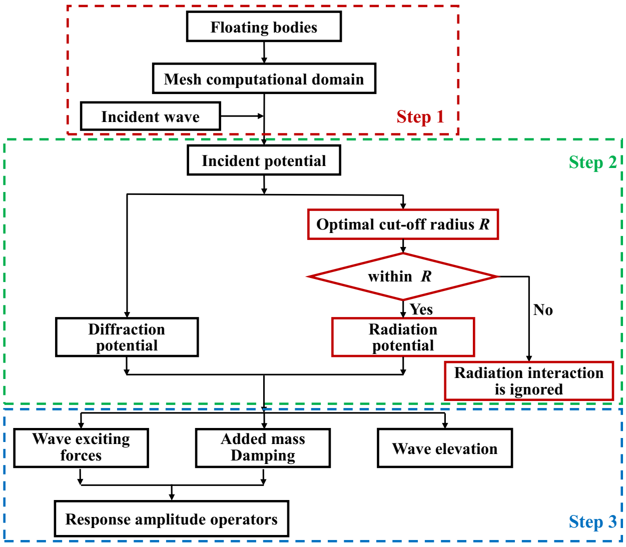

Fig. ~~5~~6. Flow chart of the hydrodynamic analysis with implementation of a cut-off scheme for radiation problem.

4. Results and validations

As we have pointed out in Section 3, the cut-off radius R is a crucial parameter in the developed fast hydrodynamic modelling method. It is of particular interest to find the optimal R, which ensures a satisfactory calculation with feasible computational time. The in-house multi-body hydrodynamic interaction programme MHydro described in Section 2 will be applied to investigate the R in the present study.

4.1 Validations of the numerical tool

The validations of the numerical programme MHydro on two bodies can be found in Yuan et al. (2015), in which the experimental measurements from Kashiwagi et al. (2005) were used in the validation, and the diffraction and radiation forces showed a good agreement. However, they only validated the self-induced hydrodynamic coefficients due to the limited model test data. In the present study, the external-induced results computed by the commercial software WADAM will be used here to validate the numerical programme. WADAM is a linear potential flow solver where the free surface condition is satisfied by using a complex Green function, and the free surface is not modelled physically.

The validation models used here are three rectangular barges arranged side-by-side. The geometry of the rectangular barges is exactly the same and the principal dimensions are listed in Table 1. The transverse and longitudinal distance between the adjacent barges are 1.5 *m* and 0 *m* respectively. The panel distribution and computational domain of the present validation case is shown in Fig. 67. Fig. 7 8 and Fig. 8 9 show the comparison of the external-induced hydrodynamic coefficients between the present numerical programme MHydro and WADAM results. The added mass and damping coefficients are non-dimensionalized by using the mass of the rectangular barge and the product of the mass and wave frequency, respectively. Very satisfactory agreement is achieved between the present method and WADAM solution, indicating the free-surface mesh size and computation domain are set reasonably and the present numerical programme is applicable to predict the hydrodynamic interactions among multiple floating bodies. More spikes are observed in the hydrodynamic coefficients of B_1 induced by the motion of B_3 than that induced by B_2. This is due to the fact that when we calculate A^{13} or B^{13}, the radiated waves generated by B_3 are modified due to the presence of B_2 before they approach B_1. The waves at B_1 are the superposition of the radiation (B_3) and diffraction waves (B_2), which makes the hydrodynamic interaction between B_1 and B_3 more complicated. On the other hand, when we calculate A^{12} or B^{12}, the presence of B_3 (treated as fixed body) will also modify the waves at B_1, considering the distance between B_1 and B_3, the effect is smaller.

Table 1 Main dimensions of the rectangular barge.

	Rectangular Box
Length	$L = 2\ m$
Breadth	$B = 0.3\ m$
Draught	$T = 0.125\ m$
Displacement	$V = 0.75\ t$
Water-plane area	$A_w = 0.60\ m^2$

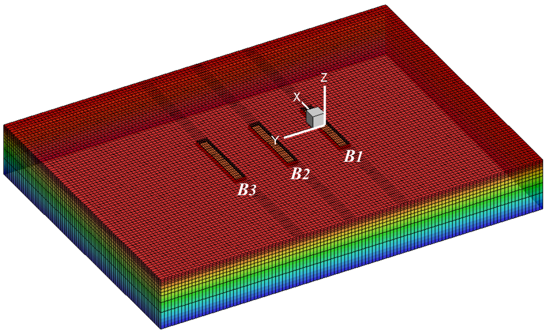

Fig. ~~6~~ 7. Computational domain of the validation model in beam wave. The free surface is truncated at 2.5L upstream, 2.5L downstream and 2L sideward. There are 380 panels on each body surface, 9080 on the free surface and 3800 on the control surface.

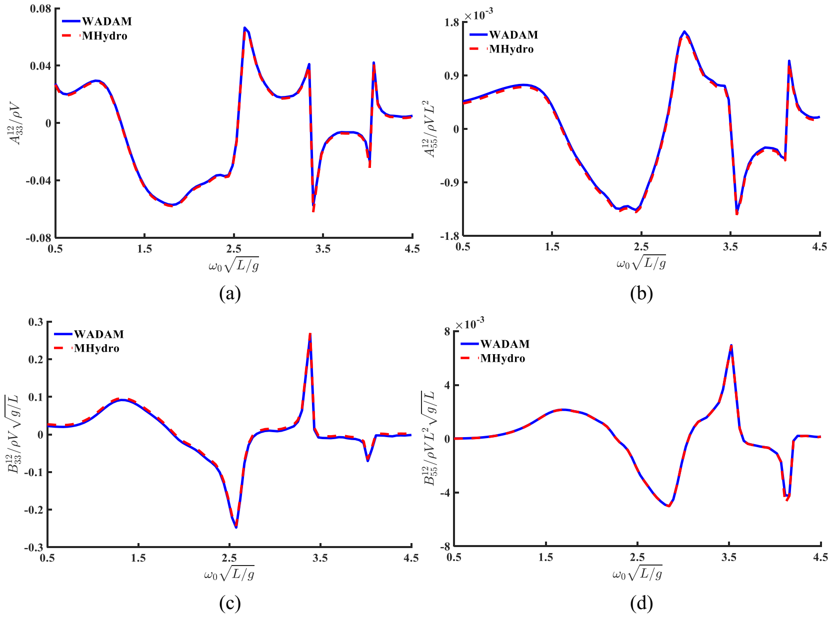

Fig. ~~7~~ 8. Hydrodynamic coefficients of B_1 due to the motion of the B_2. (a) Heave-induced heave added mass; (b) Pitch-induced pitch added mass; (c) Heave-induced heave damping; (d) Pitch-induced pitch damping.

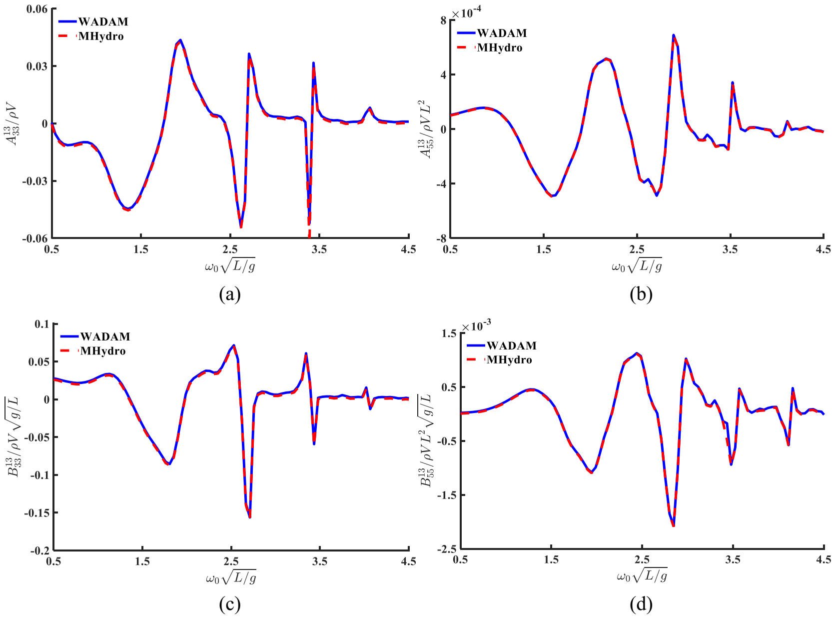

Fig. 8 9. Hydrodynamic coefficients of B_1 due to the motion of the B_3. (a) Heave-induced heave added mass; (b) Pitch-induced pitch added mass; (c) Heave-induced heave damping; (d) Pitch-induced pitch damping.

4.2 Case study

4.2.1 Numerical models

After the validation, the programme MHydro can be used to evaluate the optimal cut-off radius R. As mentioned in Section 3, the optimal R can be found by massive numerical calculations of two modularized floating bodies with the same shape. Thus, two typical case studies, based on side-by-side square boxes with a diameter $L = 1m$, are designed to verify this assumption. As shown in Fig. 910, the only difference between these two cases is that a third box is placed at the midline of the gap in the second case.

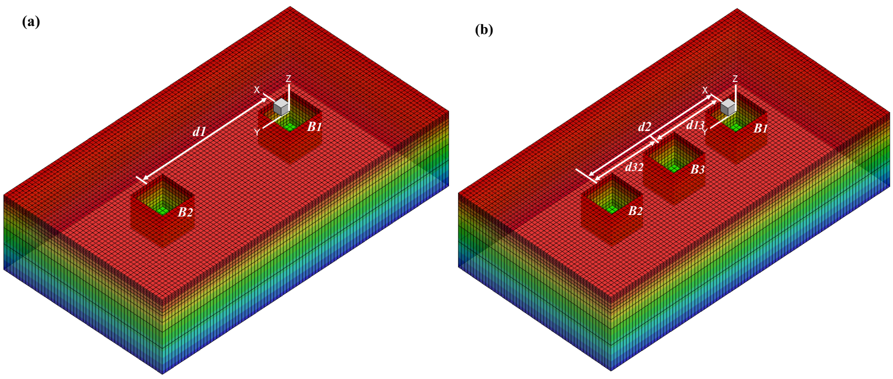

Fig. ~~9~~10. Computational domain and panel distribution of the numerical models. The free surface is truncated at 2.5L upstream, 2.5L downstream, and 2.5L sideward. (a) Two boxes system with $d1$=4L; (b) three boxes system with $d2$=4L, $d13$=$d32$=2L.

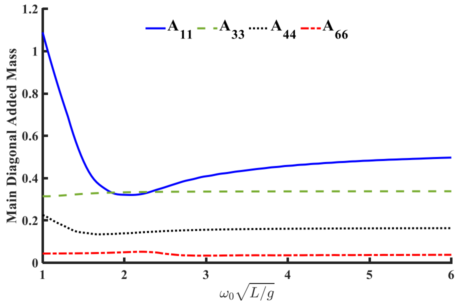

Fig. ~~10~~11. Added mass of the single square box. The non-dimensionalization for added mass with 11, 22, 33 is made by ρV; the subscript of 44, 55, 66 is made by $\rho V L^2$.

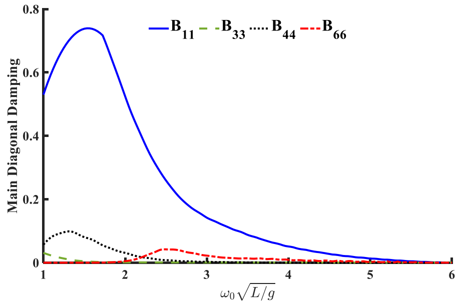

Fig. ~~11~~12. Damping of the single square box. The non-dimensionalization for damping with 11, 22, 33 is made by $\rho V\sqrt{g/L}$; the subscript of 44, 55, 66 is made by $\rho V L^2\sqrt{g/L}$.

The hydrodynamic coefficients obtained from the numerical simulations can represent the hydrodynamic properties of a single box, as presented in Fig. ~~10~~ 11 and Fig. ~~11~~12. According to the symmetrical properties of the square box, the hydrodynamic coefficients are the same in surge and sway, pitch and roll, respectively. However, for a side-by-side floating bodies system, a more sophisticated parameter should be used to estimate the effect of hydrodynamic interactions. This parameter can be either A_{ij}^{mn}/A_{ij}^{S} or B_{ij}^{mn}/B_{ij}^{S}, which is the external-induced hydrodynamic coefficient non-dimensionalized by the single body results. The superscript 'mn' represents the radiation interaction between the m- and n-th body, while superscript "S" is referred to as the single body results. Obviously, a larger ratio indicates a stronger interaction between B_m and B_n. As we can see from Fig. ~~11~~12, the hydrodynamic damping coefficients turn to be near-zero values as the wave frequency increases, indicating the damping coefficients of a single body are not suitable to be used as the denominator. This is not the case for the added mass coefficients. Therefore, we use A_{ij}^{mn}/A_{ij}^{S} represent the radiation interaction in the present study.

The results of hydrodynamic interaction are shown in Fig. ~~12~~13. Generally, the external-induced hydrodynamic coefficients gradually decay as the wave frequency increases, which indicates that the oscillation of B_2 could hardly influence the hydrodynamic properties of B_1 at the high frequency range. Some spikes can also be observed in Fig. ~~12~~13, and even a few negative values. The results in Fig. ~~13~~ 14 can be used to explain this phenomenon of negative added mass. As shown in Eq. (16) and Eq. (19), the added mass coefficients and the real part of the wave elevation are related to the imaginary part of the velocity potentials. Fig. ~~13~~ 14 (a) shows the real part of radiated wave patterns and wave profiles of the two-box system at $\omega_0\sqrt{L/g}$=1.41 and 1.66, corresponding to the negative and positive peaks of the curve respectively. Meanwhile, the radiated wave patterns and wave profiles of the three-box system at $\omega_0\sqrt{L/g}$=1.34 and 1.57 are presented in Fig. ~~13~~ 14 (b). Because of the symmetrical property of the wave field about *y*-axis, the radiated waves produced by the unit sway of B_2 are also symmetrical about *y*-axis. From the upper-half contours and black solid curves in Fig. ~~13~~ 14 (a) and (b), we can find that the wave elevation at the starboard of B_1 is much higher than that at the portside. This explains why the added mass in sway is negative in these cases. The lower-half contours and red sold curves in Fig. ~~13~~ 14 show the opposite performance, which explains why the added mass is positive in these cases. However, the external-induced hydrodynamic coefficients presented in Fig. ~~12~~ 13 (b) differ a lot from those shown in Fig. ~~12~~ 13 (a) due to the existence of B_3. Fig. ~~14~~ 13 shows the radiated wave patterns of two cases at the same wave frequency. It can be observed that the wave elevation at the portside weather side of the B_1 shown in the lower half of Fig. ~~14~~ 15 (a) is much lower than that in the upper half, which explains why the external-induced added mass shown in Fig. ~~12~~ 13 (b) has a lower trough at $\omega_0\sqrt{L/g}$=1.95. Meanwhile, from Fig. ~~14~~ 13 (b) we can also find that at high frequency range, the presence of B_3 is acting as a role of breakwater, absorbing the waves generated by B_2. As a results, less waves are transmitted to the downstream of B_3, leading to less interactions at B_1.

As described in Section 3, a *Et* must be set to find the corresponding optimal cut-off radius. If the value of A_{ij}^{mn}/A_{ij}^{S} is less than a given Et, the radiation interaction between the *m*- and *n*-th body can be ignored in the calculation. *Et*=5% is chosen as an example in Fig. ~~12~~ 13 to explain how to quantify the optimal cut-off radius *R*. As can be seen from Fig. ~~12~~ 13 (a), the results of A_{ij}^{12}/A_{ij}^{S} are less than the 5% *Et* at oscillating frequency $\omega_0\sqrt{L/g}$>3.32, which indicates that the radiation interactions between B_1 and B_2 in the two-box system can be ignored at $\omega_0\sqrt{L/g}$>3.32. For the three-box system, the radiation interactions between B_1 and B_2 can be ignored at $\omega_0\sqrt{L/g}$>3.16, when the truncation error is given at 5%. Due to the existence of B_3, the cut-off frequency in Case 2 is smaller than that in Case 1. It indicates the frequency range in which the radiation radiations can be ignored will be shrunk by the existence of other bodies.

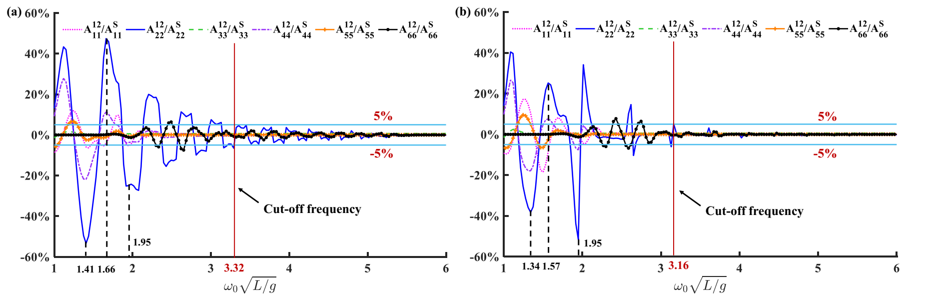

Fig. ~~12~~13. External-induced added mass of the identical square box with the transverse distance of *d*=4*L*. (a) Two-box system; (b) three-box system. The results are non-dimensionalized by the corresponding values of the single square box.

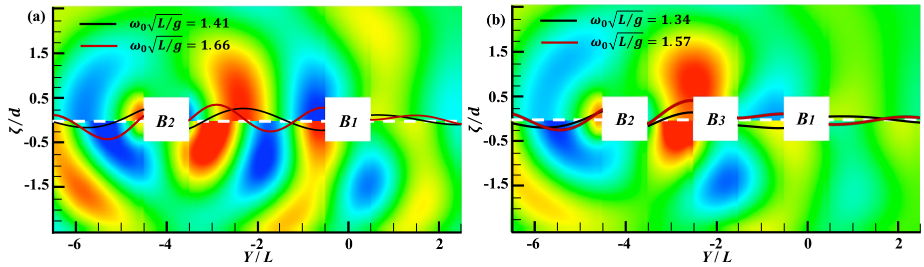

Fig. ~~13~~14. Real part of radiated waves for unit sway of B_2. The results are non-dimensionalized by the transverse distance d between B_1 and B_2. The background contours represent the wave patterns, and the solid curves are the wave profiles at the centre line. (a) Two-box system. Upper half: waves generated at $\omega_0\sqrt{L/g}$=1.41. Lower half: waves generated at $\omega_0\sqrt{L/g}$=1.66. Black curve: wave profile at the centre line at $\omega_0\sqrt{L/g}$=1.41. Red curve: wave profile at the centre line at $\omega_0\sqrt{L/g}$=1.66. (b) Three-box system. Upper half: waves generated at $\omega_0\sqrt{L/g}$=1.34. Lower half: waves generated at $\omega_0\sqrt{L/g}$=1.57. Black curve: wave profile at the centre line at $\omega_0\sqrt{L/g}$=1.34. Red curve: wave profile at the centre line at $\omega_0\sqrt{L/g}$=1.57.

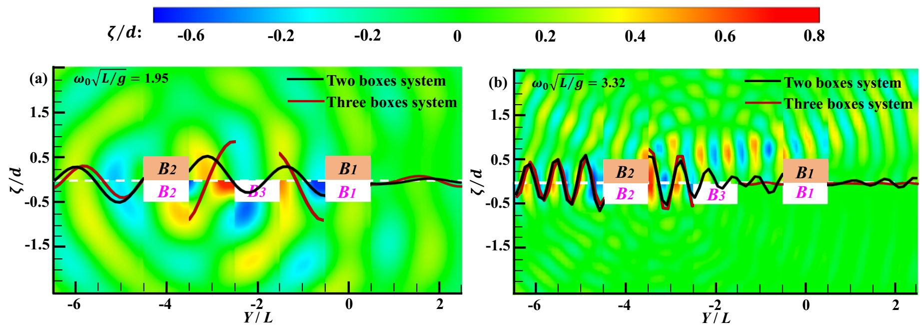

Fig. ~~14~~15. Real part of radiated waves for unit sway of B_2. The results are non-dimensionalized by the transverse distance d between B_1 and B_2. The background contours represent the wave patterns. Upper half: waves generated by B_2 in two-box system. Lower half: waves generated by B_2 in three-box system. The solid curves are the wave profiles at the centre line. Black solid curves: wave profiles in two-box system. Red solid curves: wave profiles in three-box system. (a) $\omega_0\sqrt{L/g}$=1.95. (b) $\omega_0\sqrt{L/g}$=3.32.

4.2.2 *Effects of relative angular position*

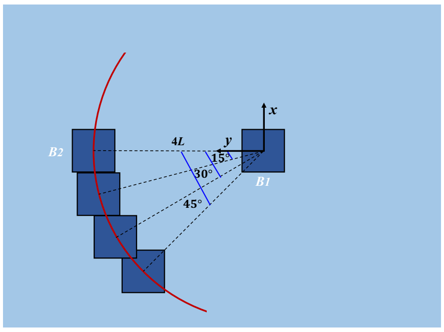

Fig. ~~15~~16. Four configurations of two boxes system.

Table 2 Cut-off wave frequency of two boxes system with various relative position angles.

Relative position angle	0°	15°	30°	45°
Cut-off frequency $\omega_0\sqrt{L/g}$	3.32	2.96	2.87	2.81

Varying the angle between the horizontal centre axis of the two boxes from 0° to 45° with an increment 15°, we can figure out the effect of angular position. The separating distance between the two boxes is fixed at $4L$. Four layout configurations are shown in Fig. ~~15~~16. Table 2 presents the results of the cut-off frequency with different angles. From the results, it can be found that the wave frequency shift to lower values with the increase of relative position angle. It indicates as the relative angle increases, the frequency range with evident radiation interactions will shrink. Therefore, the hydrodynamic interactions between two side-by-side boxes are the most intensive one, which can be selected as a typical case to investigate the optimal cut-off radius problem in the present study.

4.3 Optimal cut-off radius diagram

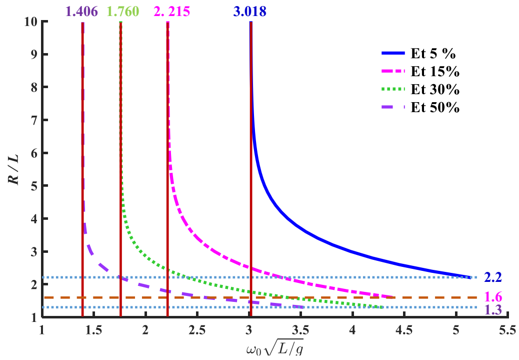

Fig. ~~16~~17. Critical curves showing whether the hydrodynamic interaction effects can be ignored.

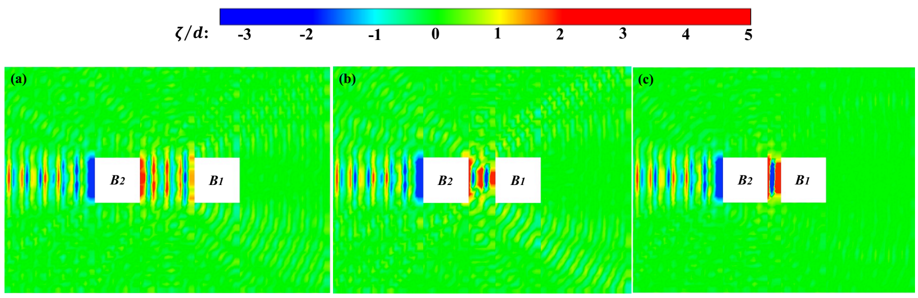

Fig. ~~17~~18. Real part of radiated waves induced by the unit sway motion of B_2 at $\omega_0\sqrt{L/g}$=5.2. (a) Transverse distance *d*=2.2*L*; (b) transverse distance *d*=1.6*L*; (c) transverse distance *d*=1.3*L*.

Apart from frequency, the separation distance is another parameter which affects the hydrodynamic interaction. Obviously, a smaller distance will lead to a larger interaction. If the distance and *Et* are provided, one can always find a unique cut-off wave frequency. Based on this assumption, we can design a large computational matrix to obtain the cut-off wave frequency at various combination of distance and *Et*, thereby quantifying the coherence of these three parameters: distance, error, frequency. With truncation errors of 5%, 15%, 30% and 50% as examples, the critical curves can be obtained and presented in Fig. ~~16~~17. These curves can be fitted with Eq. (22), where the corresponding parameters are listed in Table 3. Based on the curves in Fig.~~16~~17, an interpolation can help to obtain the combination of frequency and distance at any truncation errors. Each critical curve in Fig. ~~16~~ 17 can divide the distance-frequency plane into two domains: lower-left domain and upper-right domain. When the combination of distance and frequency is located in the upper-right domain, the radiation interaction effects between the *m*- and *n*-th bodies can be ignored in the calculations. Otherwise, the interactions need be considered. As the *Et* increases, the frequency corresponding to the longitudinal asymptote gradually decreases. It indicates that the optimal *R* associated with the larger *Et* can be introduced over a broader frequency range to reduce more computational time.

Fig. ~~16~~ 17 shows that the critical lines associated with the various truncation errors have the same trend. As the wave frequency increases, the optimal cut-off radius shows a dramatic decrease and then gradually converges to a minimum cut-off radius. It can be found that for any given *Et*, we can always find a minimum cut-off radius. As can be seen in Fig. ~~17~~18, the sway-induced wave elevation in the gap is much higher than that at the starboard of B_1. It indicates that most of the radiation wave energy is not transmitted to the downstream side of B_1 at such high frequency. Most of the waves are reflected and trapped in the gap between two bodies, particularly when the floaters are getting very close to each other. Consequently, it may induce a large wave load on both floaters, which explains why a minimum cut-off radius need to be defined in the present scheme. As the separating distance decreases, the wave elevation in the gap becomes higher and more focused, which indicates that the greater wave loads will be produced on the boxes. This explains why the critical line with a larger truncation error tends to a smaller minimum cut-off radius.

$$\omega_0\sqrt{L/g} = a \times e^{-b\times(R/L)} + c \tag{22}$$

Table 3 Parameters in the formulas of the cut-off interaction coupling radius.

Et	a	b	c
5%	18.83	0.99	3.02
15%	13.07	1.12	2.22
30%	18.14	1.52	1.76
50%	27.41	1.96	1.39

4.4 Validations of the developed cut-off scheme

The developed cut-off scheme makes it feasible to save computational time in solving the radiation interaction among the modularized floating bodies in large arrays. The optimal cut-off radius obtained in Section 4.3 is used here to perform the hydrodynamic analysis of the array, and the hydrodynamic results are compared with direct simulations without a cut-off. Two validation cases are designed here to examine the accuracy and efficiency of the proposed cut-off scheme. The array configurations and panel distributions are shown in Fig. ~~18~~19. The difference between these two validation cases is the transverse distance between the adjacent boxes: 2L for Case 1 and 1.5L for Case 2. The free surface is truncated at *2.5L* upstream, *2.5L* downstream, and *2L* sideward. In both validation cases, the incident wave direction is 0°, and the range of the incident wavelength is given as $\lambda/L = 0 \sim 5$.

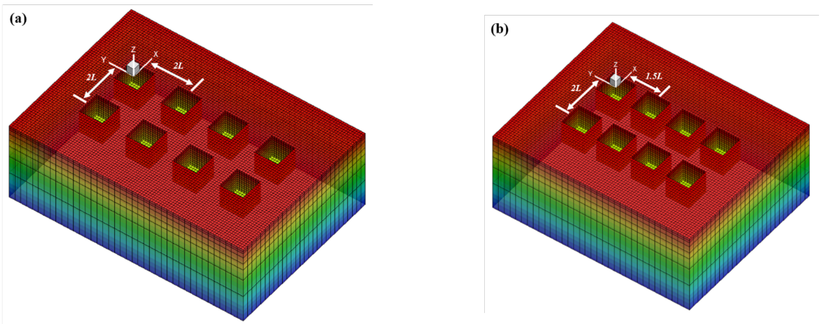

Fig. ~~18~~19. Computational domain and panel distribution of the numerical model. The free surface is truncated at 2.5L upstream, 2.5L downstream, and 2L sideward. (a) Validation case 1: the transverse distance between the adjacent boxes is 2L. There are 500 panels on each body surface, 6200 panels on the free surface and 1088 panels on the control surface; (b) Validation case 2: the transverse distance between the adjacent boxes is 1.5L. There are 500 panels on each body surface, 5150 panels on the free surface and 992 panels on the control surface.

4.4.1 Radiation hydrodynamic coefficients

Fig. ~~19~~ 20 and Fig. ~~20~~ 21 show the total hydrodynamic coefficients with different truncation errors in the two validation cases. The total hydrodynamic coefficients obtained by using the superposition method consist of self-induced components and external-induced components. To ensure the reliability of validations, the results considering the full interactions among 8 boxes are compared with WADAM solutions. The agreement between the present calculations (*Et*=0%) and WADAM results is very satisfactory, which indicates the present programme is capable to predict the full hydrodynamic interactions. Special attention should be paid on the results considering no interaction (*Et*=100%) among boxes. It can be clearly observed that there are evident discrepancies between the results with or without interaction effects, particularly at lower frequencies, where the radiation interactions are intensive. When the interaction is partly considered in the form of a *Et*, the discrepancies become smaller. When the *Et* reduced to 5% and 15%, the discrepancies can hardly be observed. It indicates that the proposed cut-off scheme is capable to predict the radiation interaction problem with a satisfactory accuracy and a reduced computational time. Fig. ~~21~~ 22 presents the relative errors and computational time ratios. The relative errors in the calculations are defined as

$$Er = \frac{1}{n}\sum^{n} \frac{|R_C - R_F|}{|R_F|} \times 100\% \tag{23}$$

where n is the number of wave frequency, R_C is the results predicted by the proposed cut-off scheme and R_F is the results considering the full interactions.

The time saving of the proposed approach is qualified by the computational time ratio, which can be defined as

$$C_t = \frac{t_C}{t_F} \times 100\% \tag{24}$$

Where t_C is the computational time consumed by the proposed cut-off scheme and t_F is the time required for considering the full interactions.

Obviously, a smaller *Et* is always accompanied by a higher accuracy, but requires more computational time. In engineering practice, a suitable *Et* needs to be determined to achieve a balance between the computational accuracy and efficiency. In both cases, the relative errors of damping are larger than those of added mass. The reason is that the optimal *R* used in these cases is obtained by quantifying the external added mass coefficients A_{ij}^{mn}/A_{ij}^{S}. At the 15% *Et*, the relative errors in Case 2 are significantly smaller. The reason can be found in Fig. ~~22~~ 23 (b). B_2 and B_6 are located within the minimum cut-off radius at *Et*= 15%. However, they are outside the minimum cut-off radius in Case 1, which can be observed in Fig. ~~22~~ 23 (a). From Fig. ~~21~~ 22 it can be found that more than 50% of the computational time could be saved, even if *Et*=5% is selected. It shows that the developed cut-off scheme is computational effective when modelling large arrays of modularized floating structures. Since the ratio of panel number on each body surface to the total panel number in Case 2, it has a better performance in terms of computational efficiency.

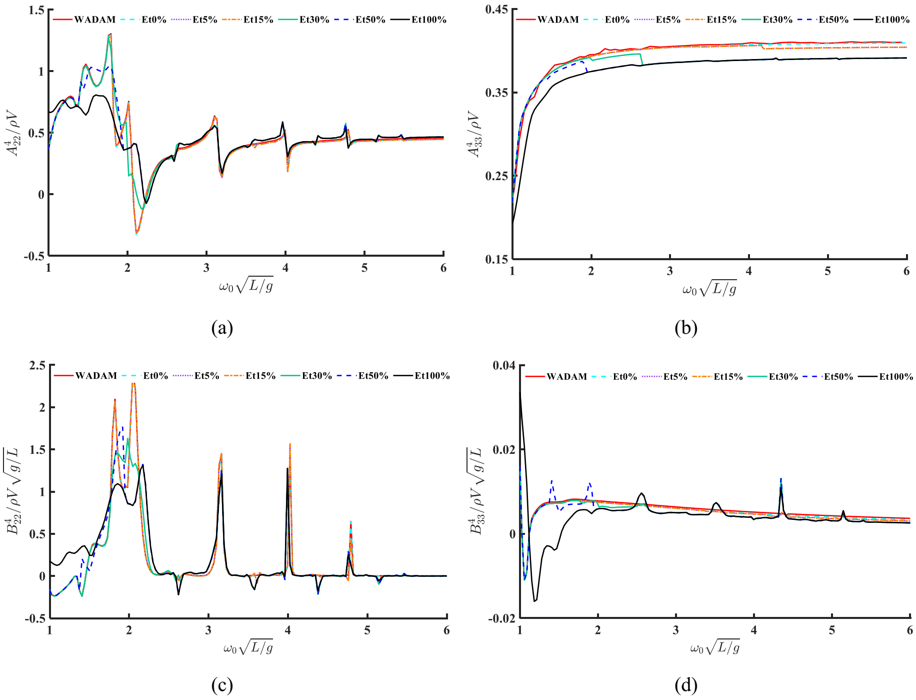

Fig. ~~19~~20. Hydrodynamic coefficients with different truncation errors of Validation case 1. (a) Sway-induced surge added mass; (b) Heave-induced heave added mass; (c) Sway-induced surge damping; (d) Heave-induced heave damping.

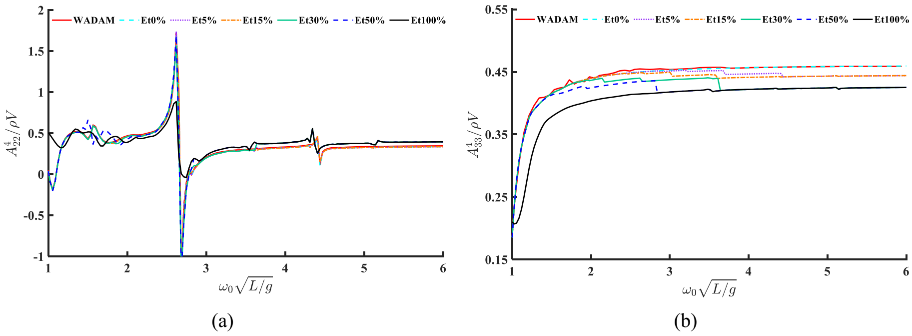

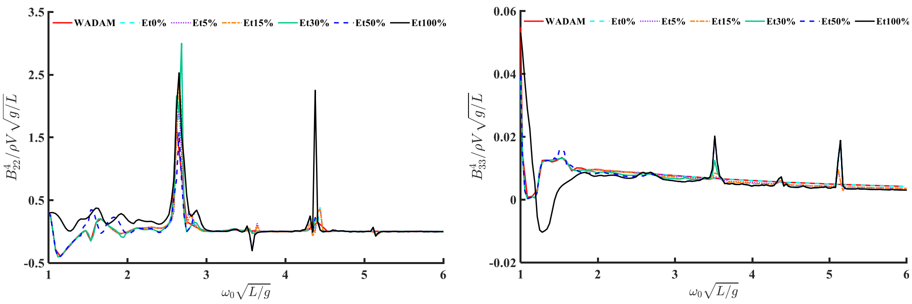

(c) (d)

Fig. ~~20~~21. Hydrodynamic coefficients with different truncation errors of Validation case 2. (a) Sway-induced surge added mass; (b) Heave-induced heave added mass; (c) Sway-induced surge damping; (d) Heave-induced heave damping.

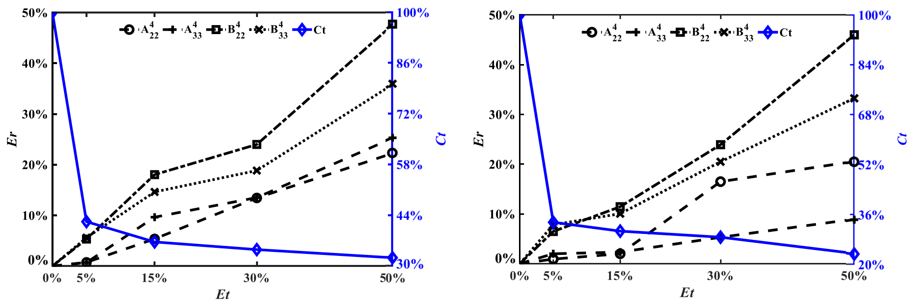

(a) (b)

Fig. ~~21~~22. Relative errors and computational time ratio. (a) Validation case 1; (b) Validation case 2.

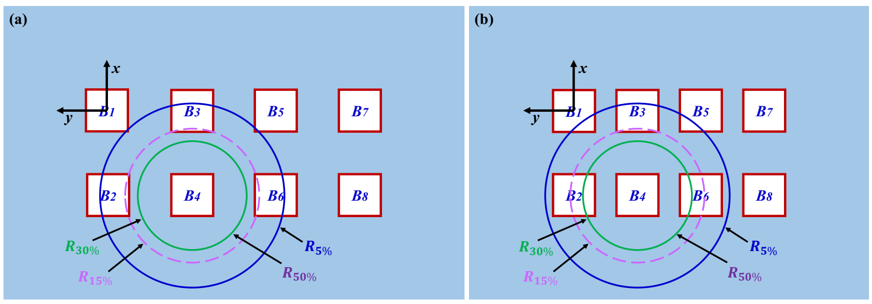

Fig. ~~22~~23. Minimum cut-off radius associated with different truncation errors. (a) Validation case 1; (b) Validation case 2.

4.4.2 Motion responses

The intensity of the hydrodynamic interaction can be represented either by A_{ij}^{mn}/A_{ij}^{S} or B_{ij}^{mn}/B_{ij}^{S}. However, the operational safety and power extraction of the large arrays are closely related to the motion responses of each floater. It would be interesting to investigate how the hydrodynamic interaction affects the motion responses of the multibody system. Fig. ~~23~~ 24 is the motion response amplitude operators (RAO) of two validation cases. Similarly, there is a large discrepancy between the results with or without consideration of the radiation interaction, particularly at long waves (or lower frequencies). However, the general agreement between the present cut-off scheme and the direct simulation with full consideration of hydrodynamic interaction effects is still very satisfactory even *Et*= 30% is applied, which indicates the proposed cut-off scheme can provide a reliable prediction of the motion responses of large arrays of modularized structures. To quantify the accuracy of the present scheme, the relative errors are analyzed and presented in Fig. ~~24~~25. A larger *Et* will result in a large *Er* in all degrees of freedom. Compared to the relative error of the calculated hydrodynamic coefficients (as shown in Fig.~~21~~22), the relative errors *Er* in motion responses are much smaller. Even when *Et*=50% is applied in the cut-off scheme, the induced calculation error of motion responses is always below 20%. As shown in Eq. (18), the truncation scheme only affects μ_{ij}^{mn} and λ_{ij}^{mn}, while the remaining terms keep unchanged. The effect of *Et* on hydrodynamic coefficients are mitigated by these unchanged terms in the motion equation. There is a big space to tune the *Et* to saving large amount of computational time while maintaining a satisfactory accuracy.

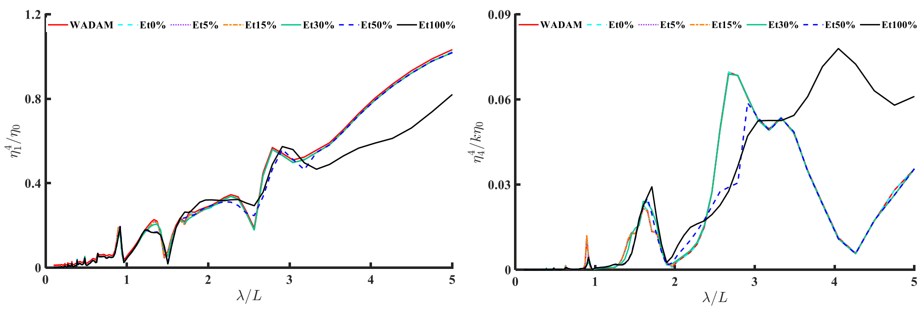

(a) (b)

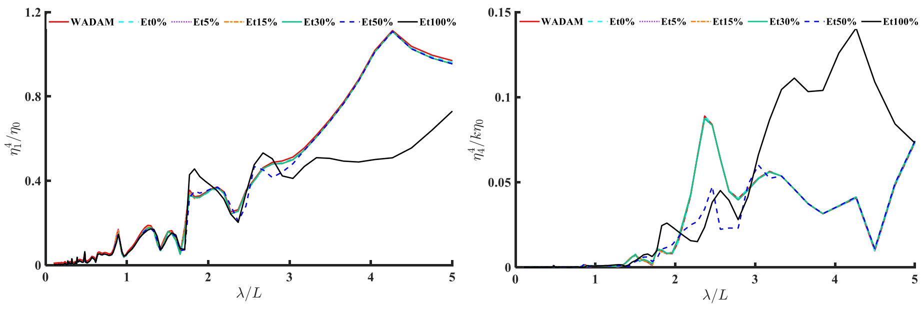

(c) (d)

Fig. ~~23~~ 24 Response amplitude operators of motion responses of B_4. (a) Surge, validation case 1; (b) roll, validation case 1; (c) surge, validation case 2; (d) roll, validation case 2.

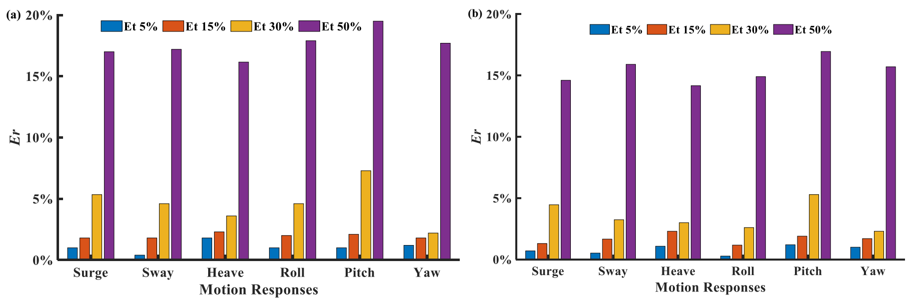

Fig. ~~24~~ 25 Relative errors of motion responses. (a) Case 1; (b) Case 2.

5. Conclusions

The present study proposes a novel cut-off scheme, which can be implemented to the multi-body hydrodynamic interaction solvers to save the computational time when modelling large arrays of modularized floating structures. To find the optimal cut-off radius, we performed extensive numerical simulations on two modularized floating boxes. Based on these calculations, the following conclusions can be drawn:

1) The cut-off radius is highly dependent on the hydrodynamic interaction effect. It is mainly determined by three parameters: separating distance, frequency, and truncation error. At lower frequencies, a large cut-off radius is required to account for the hydrodynamic interaction. A large truncation error would require a smaller cut-off radius.
2) For any given frequency and truncation error, we can always determine a cut-off radius, out of

which the hydrodynamic interaction effects can be ignored. Some critical curves can be obtained, which can divide the distance-frequency plane into two distinct domains. From these curve, one can easily determine the cut-off radius.

3) With the implement of the cut-off scheme, the hydrodynamic interaction can be well predicted, particularly when a small truncation error is applied. At *Et*=5%, the computational time of the cut-off scheme is only 40% of the direct simulation with full consideration of the radiation interaction.
4) The motion responses of the floaters in an array are less sensitive to the truncation error. Even when *Et*=50% is applied in the cut-off scheme, the error in the calculated motion responses is still below 20%.

Acknowledgements

This study is supported by the National Natural Science Foundation of China (No. 52088102 and No. 51979131) and the China Scholarship Council Foundation References.

References

Borgarino, B., Babarit, A., Ferrant, P., 2012a. Impact of wave interactions effects on energy absorption in large arrays of wave energy converters. Ocean Engineering, 41: 79-88.
Borgarino, B., Babarit, A., Ferrant, P., 2012b. An implementation of the fast multipole algorithm for wave interaction problems on sparse arrays of floating bodies. Journal of Engineering Mathematics, 77(1): 51-68.
Budal, K., 1977. Theory for absorption of wave power by a system of interacting bodies. Journal of Ship Research, 21(04), 248-254.
Cao, Y., Schultz, W. W., Beck, R. F., 1991. Three-dimensional desingularized boundary integral methods for potential problems. International Journal for Numerical Methods in Fluids, 12(8), 785-803.
Engström, J., Eriksson, M., Göteman, M., Isberg, J., Leijon, M., 2013. Performance of large arrays of point absorbing direct-driven wave energy converters. Journal of Applied Physics, 114, 204502.
Fang, M. C., Kim, C. H., 1986. Hydrodynamically coupled motions of two ships advancing in oblique waves. Journal of Ship Research, 30(03), 159-171.
Fitzgerald, C., Thomas, G., 2007. A preliminary study of the optimal formation of an array of wave power devices, Proceedings of the 7th European Wave and Tidal Energy Conference, Porto, Portugal.
Göteman, M., Engström, J., Eriksson, M., Isberg, J., 2015. Fast Modeling of Large Wave Energy Farms Using Interaction Distance Cut-Off. Energies, 8(12): 13741-13757.
Hess, J. L., Smith, A. M. O., 1964. Calculation of nonlifting potential flow about arbitrary three-dimensional bodies. Journal of Ship Research, 8(04), 22-44.

Hong, S. Y., Kim, J. H., Cho, S. K., Choi, Y. R., Kim, Y. S., 2005. Numerical and experimental study on hydrodynamic interaction of side-by-side moored multiple vessels. Ocean Engineering, 32(7), 783-801.

Kashiwagi, M., Ohkusu, M., 1991. A new theory for side-wall interference effects on forward-speed radiation and diffraction forces. Ship Technology Research, 38(1), 17-48.

Kodan, N., 1984. The motions of adjacent floating structures in oblique wave, Proceeding Conference of the 3rd International Offshore Mechanics and Arctic Engineering Symposium. New Orleans, America, pp. 206-231.

Kring, D., Korsmeyer, T., Singer, J., White, J., 2000. Analyzing mobile offshore bases using accelerated boundary-element methods. Marine Structures, 13(4-5), 301-313.

Ohkusu, M., 1976. Ship motions in vicinity of a structure, Proceedings of International Conference on Behavior of Offshore Structure. Trondheim, Norway, pp. 284-306.

Penalba, M., Touzón, I., Lopez-Mendia, J., Nava, V., 2017. A numerical study on the hydrodynamic impact of device slenderness and array size in wave energy farms in realistic wave climates. Ocean Engineering, 142: 224-232.

Prins, H. J., 1995. Time Domain Calculations of Drift Forces and Moments (Ph.D. thesis). Delft University of Technology, The Netherlands.

Rodrigues, J. M., 2021. A Procedure to Calculate First-Order Wave-Structure Interaction Loads in Wave Farms and Other Multi-Body Structures Subjected to Inhomogeneous Waves. Energies, 14(6), 1761.

Simon, M. J., 1982. Multiple scattering in arrays of axisymmetric wave-energy devices. Part 1. A matrix method using a plane-wave approximation. Journal of Fluid Mechanics, 120, 1-25.

Singh, J., Babarit, A., 2014. A fast approach coupling Boundary Element Method and plane wave approximation for wave interaction analysis in sparse arrays of wave energy converters. Ocean Engineering, 85: 12-20.

Teng, B., Gou, Y., 2006. Fast multipole expansion method and its application in BEM for wave diffraction and radiation, Proceedings of the 16th International Offshore and Polar Engineering Conference. pp. 318–325.

Utsunomiya, T., Watanabe, E., 2002. Accelerated higher order boundary element method for wave diffraction/radiation problems and its applications, Proceedings of the 12th International Offshore and Polar Engineering Conference. pp. 305–312.

Yang, S.-H., Ringsberg, J. W., Johnson, E., 2020. Wave energy converters in array configurations—Influence of interaction effects on the power performance and fatigue of mooring lines. Ocean Engineering, 211, 107294.

Yuan, Z.-M., Incecik, A. and Alexander, D., 2014. Verification of a new radiation condition for two ships advancing in waves. Applied Ocean Research, 48: 186-201.

Yuan, Z.-M., Incecik, A., Dai, S., Alexander, D., Ji, C.-Y., Zhang, X., 2015. Hydrodynamic interactions between two ships travelling or stationary in shallow waters. Ocean Engineering, 108: 620-635.

Yuan, Z.-M., Ji, C.-Y., Incecik, A., Zhao, W., Day, A., 2016. Theoretical and numerical estimation of ship-to-ship hydrodynamic interaction effects. Ocean Engineering, 121: 239-253.

Zhu, H. R., Zhu, R. C., Miao, G. P., 2008. A time domain investigation on the hydrodynamic resonance phenomena of 3-D multiple floating structures. Journal of Hydrodynamics, 20(5), 611-616.

Page 9: [1] Formatted Deqing Zhang 03/10/2022 05:45:00

Font: (Asian) +Body Asian (DengXian), English (UK), Pattern: Clear